Linear Modes for Channels of Constant Cross-Section and Approximate Dirichlet–Neumann Operators

R. M. Vargas-Magaña[1] · **P. Panayotaros**[2] · **A. A. Minzoni**[2]

Abstract

We study normal modes for the linear water wave problem in infinite straight channels of bounded constant cross-section. Our goal is to compare semi-analytic normal mode solutions known in the literature for special triangular cross-sections, namely isosceles triangles of equal angle of 45° and 60°, see Lamb (Hydrodynamics. Cambridge University Press, Cambridge, 1932) , Macdonald (Proc Lond Math Soc 1:101–113, 1893), Greenhill (Am J Math 97–112 , 1887), Packham (Q J Mech Appl Math 33:179–187, 1980), and Groves (Q J Mech Appl Math 47:367–404, 1994), to numerical solutions obtained using approximations of the non-local Dirichlet–Neumann operator for linear waves, specifically an ad-hoc approximation proposed in Vargas-Magaña and Panayotaros (Wave Motion 65:156–174, 2016), and a first-order truncation of the systematic depth expansion by Craig et al. (Proc R Soc Lond A: Math, Phys Eng Sci 46:839–873, 2005). We consider cases of transverse (i.e. 2-D) modes and longitudinal modes, i.e. 3-D modes with sinusoidal dependence in the longitudinal direction. The triangular geometries considered have slopping beach boundaries that should in principle limit the applicability of the approximate Dirichlet–Neumann operators. We nevertheless see that the approximate operators give remarkably close results for transverse even modes, while for odd transverse modes we have some discrepancies near the boundary. In the case of longitudinal modes, where the theory only yields even modes, the different approximate operators show more discrepancies for the first two longitudinal modes and better agreement for higher modes. The ad-hoc approximation is generally closer to exact modes away from the boundary.

Keywords Linear water waves · Whitham–Boussinesq model over variable topography · Dirichlet–Neumann operator · Normal modes on triangular straight channels · pseudodifferential operators

---

A. A. Minzoni: Deceased.

✉ R. M. Vargas-Magaña
  rmvargas@ciencias.unam.mx

1   Mathematical Sciences Research Institute, 17 Gauss Way, Berkeley 947205070, CA, USA

2   Departamento de Matemáticas y Mecánica IIMAS, Universidad Nacional Autónoma de México, Apdo. Postal 20-726, 01000 Mexico City, Mexico

🕮 Birkhäuser

1 Introduction

We study some problems on normal modes in the linear water wave theory, in particular we compute transverse and longitudinal normal modes in infinite straight channels of constant bounded cross-section, considering special depth profiles for which there are known explicit or semi-explicit analytical solutions in the literature [13,14,21,23,28]. We compare the results to numerical normal modes obtained using simple approximations of the nonlocal variable depth Dirichlet–Neumann operator for the linear water wave equations, in particular a recently proposed ad-hoc approximation [32], as well as a first-order truncation of the systematic expansion in the depth proposed by Craig, Guyenne, Nicholls and Sulem [7]. Our main motivation is to test the simple approximations to the Dirichlet–Neumann operator as they are of interest in constructing simplified nonlocal shallow water models, e.g. Whitham–Boussinesq equations [1,4,18,25], and arXiv:1608.04685 by Hur, and Pandey. Such models have attracted considerable current interest [5,10,11,19,27], and arXiv:1602.05384 by Ehrnstrom and Wahlén. The inclusion of variable depth effects raises additional questions on the dynamics of these systems and is of interest in geophysical and coastal engineering applications.

The nonlocal linear system we use to compute normal modes is derived using the Hamiltonian formulation of the free surface potential flow [35], see also [24,31], and approximations for the (nonlocal) Dirichlet–Neumann operators for the Laplacian in the fluid domain appearing in the kinetic energy part of the Hamiltonian [6]. Explicit infinite series expressions for the Dirichlet–Neumann operator in variable depth were derived by Craig, Guyenne, Nicholls and Sulem [7], see also [22]. Such expressions are generally complicated and can be used for numerical computations [15], or to further simplify the equations of motion. The Dirichlet–Neumann operator can be computed numerically using alternative formulations that can be generalized to variable depth, see [34] for a comparison of several methods. Also, water waves over variable depth have been studied using a Hamiltonian coupled mode formulation that is based on the construction of bases for the potential in the fluid domain and the variational formulation of free surface potential flow [29]. Ad-hoc approximations for the dispersion combined with variational formulations were used by [30] for linear waves and [3,29] for nonlinear waves.

The Hamiltonian and Dirichlet–Neumann formulation implies that variable depth effects are already captured at the level of the linear theory, i.e. the nontrivial wave-amplitude operator is expressed recursively in terms of the linear operator [7,8]. The study of linear normal modes is, therefore, a good test problem for comparing different approximations of the Dirichlet–Neumann operator for variable depth. In this paper we focus on simple approximations of the variable depth operator, such as the ad-hoc generalization of the constant depth operator for arbitrary depth proposed in [32]. This operator has some of the structural properties of the exact Dirichlet–Neumann operator, e.g. symmetry and exact infinite depth asymptotics, but is also seen to lead to a depth expansion that differs from the exact one of [7].

The idea of the paper is compare results obtained using the approximate Dirichlet–Neumann operators to semi-analytic normal mode solutions known for some special

depth profiles. These analytical results rely on the existence of families of harmonic functions that satisfy the rigid wall boundary conditions at the bottom, and can be only obtained for a few special depth profiles, such as isosceles triangles with sides inclined at 45° and 60° to the vertical, see Greenhill [13], Macdonald [23], and the summary in Lamb's book, [21]. More recent studies are by Packham [28] and Groves [14]. A complete set of modes was also obtained for a semicircular channel by Evans and Linton [12]. The construction typically yields even and odd normal modes that we then compare to even and odd eigenfunctions of approximate Dirichlet–Neumann operators in a periodic domain.

One problem with our plan is that the non-constant depth examples with classical analytic solutions we are aware of concern domains with a slopping beach, and as we clarify below, the classical and periodic Dirichlet–Neumann approaches are not equivalent because of the different assumptions at the intersection between the horizontal and sloping beach boundaries. Despite this problem, we find that the two approaches give comparable and often very close results for the 2-D normal mode shapes, especially away from the beach. This is especially the case for even modes, where we see good agreement in the entire domain. Results for odd modes are close away from the beach, but have a marked discrepancy near the beach. In that case the periodic problem for the approximate Dirichlet–Neumann operators leads to modes that vanish at boundary, while odd exact modes have maxima at the boundary. In the problem of 3-D even longitudinal modes, we consider moderate speed along the transverse direction and see more discrepancies between the exact and approximate modes. Agreement in the interior is good after the first two modes, but discrepancies at the boundary persist for higher even modes. The approximate Dirichlet–Neumann approach also gives results for the odd case, where there are no exact results.

In summary, the approximate periodic Dirichlet–Neumann operators give better results for the transverse 2-D modes, especially in the interior.

In Sect. 4, we present evidence that the modes computed by the approximate periodic Dirchlet-Neumann operators are limiting cases of modes corresponding to a periodic depth profiles nowhere vanishing depth. This observation explains intuitively why the approximate operators cannot capture the slopping beach rigid wall boundary condition as realistically as the classical exact approach.

The organization of the paper is as follows: In Sect. 2 we formulate the water wave problem using the Dirichlet–Neumann operators and present the operators used to approximate the linear system. In Sect. 3, we formulate the classical problem of transverse and longitudinal modes for the linear theory and define analogues that use approximate Dirichlet–Neumann operators. In Sect. 4, we present our results, comparing normal modes obtained using the classical and approximate Dirichlet–Neumann approaches. In Sect. 5, we briefly discuss the results.

2 Water wave problem in variable depth and approximate Dirichlet–Neumann operators

Following the Hamiltonian formulation of the water wave problem due to Zakharov [35], see also [24,31], the Euler equations for free surface potential flow can be restated

as a Hamiltonian system in terms of the wave amplitude $\eta(x, t)$ and surface hydrodynamic potential $\xi(x, t) = \varphi(x, \eta(x, t), t)$, namely as

$$\partial_t \begin{pmatrix} \eta \\ \xi \end{pmatrix} = \begin{pmatrix} 0 & I \\ -I & 0 \end{pmatrix} \begin{pmatrix} \frac{\delta H}{\delta \eta} \\ \frac{\delta H}{\delta \xi} \end{pmatrix}, \tag{1}$$

where the Hamiltonian is expressed explicitly in terms of η and ξ as

$$H = \frac{1}{2} \int_{\mathbb{R}} (\xi G(\beta, \eta)\xi + g\eta^2) dx, \tag{2}$$

see [6], and the operator $G(\beta, \eta)$ is defined as follows: consider the elliptic problem

$$\Delta \varphi(x, y) = 0, \forall (x, y) \in \mathscr{D}_t(\eta) \tag{3}$$

$$\varphi(x, \eta(x)) = \xi(x), \forall x \in \mathbb{R}, \tag{4}$$

$$\frac{\partial \varphi}{\partial \hat{n}}(x, -h_0 + \beta(x)) = 0, \forall x \in \mathbb{R}, \tag{5}$$

in the two-dimensional (time-dependent) simply connected domain $\mathscr{D}_t(\eta) := \{(x, y) : x \in \mathbb{R}, -h_0 + \beta(x) < y < \eta(x, t)\}$. If η and ξ are sufficiently smooth and decay at infinity, then (3)-(5) admits a unique solution and we can compute the normal derivative of the solution at the surface $y = \eta$. The Dirichlet–Neumann operator $G(\beta, \eta)$ is then defined by

$$(G(\beta, \eta)\xi)(x) = (1 + (\partial_x \eta(x))^2)^{\frac{1}{2}} \nabla \varphi(x, \eta(x)) \cdot N(\eta(x)), \tag{6}$$

where $N(\eta(x)) = (1 + (\partial_x \eta(x))^2)^{-\frac{1}{2}}(-\partial_x \eta(x), 1)$, $x \in \mathbb{R}$, is the exterior unit normal at the free surface. The Dirichlet–Neumann operator $G(\beta, \eta)$ is a linear operator on ξ and is symmetric with respect to the usual L^2 inner product. Similar definitions apply to the periodic problem and to higher dimensions.

In [7], Craig, Guyenne, Nicholls and Sulem give an expansion of this operator in the presence of non-trivial bottom topography

$$G(\beta, \eta) = G_0(\beta, \eta) + G_1(\beta, \eta) + G_2(\beta, \eta) + \cdots, \tag{7}$$

where the G_j are homogeneous of degree j in η. The first terms are

$$G_0(\beta, \eta) = D \tanh(h_0 D) + DL(\beta), \tag{8}$$

$$G_1(\beta, \eta) = D\eta D - G_0 \eta G_0, \tag{9}$$

$$G_2(\beta, \eta) = \frac{1}{2}(G_0 D\eta^2 D - D^2\eta^2 G_0 - 2G_0\eta G_1), \tag{10}$$

where $D = -i\partial_x$, and $G_0 = G_0(\beta, \eta)$. We are also using the notation

$$[a(f(x)D^m)\xi](x) = \int_{\mathbb{R}} a(f(x)k^m)\hat{\xi}(k)e^{ikx} dk, \tag{11}$$

with a, f being real functions, and $\hat{\xi}(k) = \frac{1}{2\pi} \int_{\mathbb{R}} \xi(x) e^{-ikx} \mathrm{d}k$, the Fourier transform of the real function ξ.

At higher order, the G_j, $j > 2$ are similarly obtained from G_0, using a recursion formula. The recursion formula for the G_j is similar to the one obtained for a flat bottom, where $G_0 = D \tanh(h_0 D)$, see [8]. Variable depth effects are thus encoded in the operator $L(\beta)$.

The operator $L(\beta)$ can be expressed in powers of the depth variation β as $L(\beta) = \Sigma_{j=0}^{\infty} L_j(\beta)$, where the $L_j(\beta)$ are homogeneous of order j in β, and are computed recursively, see [7]. The first two terms in the expansion are

$$L_0(\beta) = 0, \tag{12}$$
$$L_1(\beta) = -\mathrm{sech}(h_0 D)\beta\, D\mathrm{sech}(h_0 D). \tag{13}$$

The first two terms of this expansion lead the first-order approximation $\mathscr{A}_1$ of the Dirichlet–Neumann operator

$$\mathscr{A}_1(\beta) = D \tanh(h_0 D) - D\mathrm{sech}(h_0 D)\beta\, D\mathrm{sech}(h_0 D) \tag{14}$$

that we use below. This operator was used recently in Craig et al. [9] to calculate bands for periodic depth variation. Higher order expansions in β have been considered in the numerical studies of [15–17]. To avoid these longer expressions in simplified nonlocal shallow water equations, [32] proposed an ad-hoc approximation $\mathscr{A}_{G_0}$ of the linear Dirichlet–Neumann operator given by

$$\mathscr{A}_{G_0}(\beta) = Sym(D \tanh(h(x)D)), \tag{15}$$

where $h(x) = h_0 - \beta(x)$. The (formal) symmetrization of a linear operator $\mathscr{A}$ in $L^2 = L^2(\mathbb{R}; \mathbb{R})$ with the (standard) inner product $\langle f, g \rangle = \int_{\mathbb{R}} f(x)g(x)\mathrm{d}$ is defined by $Sym(\mathscr{A}) = \frac{1}{2}(\mathscr{A} + \mathscr{A}^*)$, where $\mathscr{A}^*$ is the adjoint of $\mathscr{A}$ with respect to the inner product, i.e. $\langle \mathscr{A}f, g \rangle = \langle f, \mathscr{A}^*g \rangle$, for all f, g in the the domains of $\mathscr{A}$, $\mathscr{A}^*$, respectively. (It is assumed that the domain $D(\mathscr{A})$ of $\mathscr{A}$ is dense in L^2.) $\mathscr{A}$ is symmetric if $D(\mathscr{A}) = D(\mathscr{A}^*)$ and $\mathscr{A} = \mathscr{A}^*$, thus $D(\mathscr{A}) = D(\mathscr{A}^*)$ implies that $Sym(\mathscr{A})$ is symmetric.

Symmetrizing an approximate Dirichlet–Neumann operator is natural by (1), (2), e.g. $H = \frac{1}{2} \int_{\mathbb{R}} (\xi \mathscr{A}\xi + g\eta^2)$, $\mathscr{A}$ a linear operator, leads formally to the equations $\partial_t \eta = \frac{1}{2}(\mathscr{A} + \mathscr{A}^*)\xi$, $\partial_t \xi = -g\eta$. We note that $D \tanh(h(x)D)$ maps real-valued functions to real-valued funcions, see Appendix A and the next section for further details on symmetrizing this operator.

We check that $\mathscr{A}_1(\beta)$ of (14) is symmetric. To compare this operator to $\mathscr{A}_{G_0}$, we expand $D \tanh(h(x)D)$ in β to $O(\beta^2)$, and symmetrize. The result is the operator

$$\mathscr{A}_2(\beta) = D \tanh(h_0 D) + \frac{1}{2}[i\beta' \mathrm{sech}^2(h_0 D)D - \beta \mathrm{sech}^2(h_0 D)D^2$$
$$-i D\mathrm{sech}^2(h_0 D)\beta' + D^2 \mathrm{sech}^2(h_0 D)\beta], \tag{16}$$

see Appendix A. We see that operators $\mathscr{A}_1$ and $\mathscr{A}_2$ are apparently different.

The series formulation for the variable depth Dirichlet–Neumann operator applies to non-smooth depth variation and the terms in the series for the operator $L(\beta)$ are smoothing due to the presence of the operator $\mathrm{sech}(h_0 D)$ [7,17]. This behavior is already indicated by the $O(\beta)$ part in (14). A consequence is that at high frequencies we recover the constant depth operator $G(0, 0)$, under minimal assumptions on β. The matrix representation of the ad-hoc approximation $\mathscr{A}_{G_0}$ in the Fourier basis also becomes diagonal at high wave number, with diagonal entries approaching those of the infinite depth operator, see [32] for examples with smooth and piecewise constant depth profiles. However, the variable depth part seems to have weaker smoothing properties, e.g. in (16), see also Appendix A, it is smoothing for smooth β, but only relatively compact (with respect to D) for β' in L^2.

The series formulation for the variable depth Dirichlet–Neumann also applies to 3-D domains with arbitrary depth variation [7,17]. Recent alternative approaches to water waves in 3-D domains with variable depth are described in [2,29].

Let a, f be real functions and $g : \mathbb{R}^2 \to \mathbb{R}$, and let $D = (D_1, D_2)^T = -i(\partial_{x_1}, \partial_{x_2})^T$. We then define operators $a(f(x)g(D))$ by

$$[a(f(\mathbf{x})g(D))\xi](\mathbf{x}) = \int_{\mathbb{R}^2} a(f(\mathbf{x})g(\mathbf{k}))\hat{\xi}(\mathbf{k})e^{i\mathbf{k}\cdot\mathbf{x}}d^2\mathbf{k}, \tag{17}$$

with $\hat{\xi}(\mathbf{k}) = \frac{1}{(2\pi)^2} \int_{\mathbb{R}^2} \xi(\mathbf{x})e^{-i\mathbf{k}\cdot\mathbf{x}}d^2\mathbf{x}$, the Fourier transform of the function ξ on $\mathbb{R}^2$.

Letting

$$|D| = \sqrt{|D_1|^2 + |D_2|^2}, \tag{18}$$

the expansion of $L(\beta)$ up to $O(\beta^2)$ leads to the approximate Dirichlet–Neumann operator

$$\mathscr{A}_1(\beta) = [|D|\tanh(h_0\,|D|)] - [|D|\,\mathrm{sech}(h_0\,|D|)][\beta(\mathbf{x})\,|D|\,\mathrm{sech}(h_0\,|D|)]. \tag{19}$$

We will also consider the 3-D analogue of the ad-hoc operator of (15)

$$\mathscr{A}_{G_0}(\beta) = Sym[|D|\tanh(h(\mathbf{x})\,|D|)], \tag{20}$$

with $h(\mathbf{x}) = h_0 - \beta(\mathbf{x})$. The symmetrization is defined as in $\mathbb{R}$.

3 Linear modes in channels and Dirichlet–Neumann operators

We now consider the classical formulation of the problem of linear modes in channels. We use Cartesian coordinates denoted by (x, y, z), where y is directed vertically upwards, z is measured longitudinally along the channel and x is measured across the channel, see, e.g. Figs. 1 and 2

Fig. 1 Schematic of straight channel with triangular cross-sections $\Omega = \beta_{45}(x)$ and coordinate system
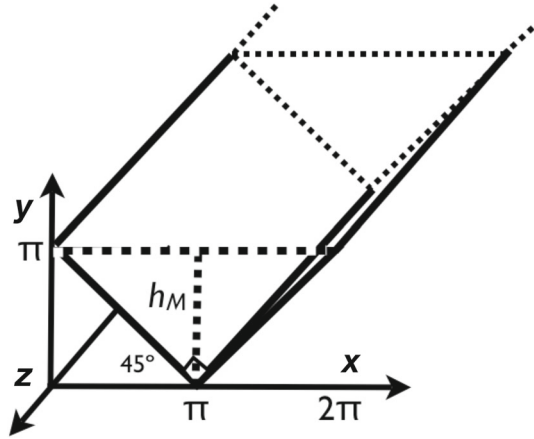
Fig. 2 Schematic of straight channel with triangular cross-sections $\Omega = \beta_{30}(x)$ and coordinate system
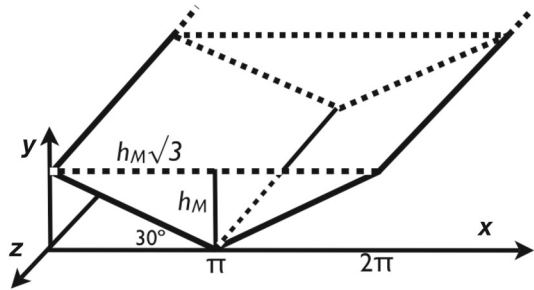
We define the fluid domain as $\mathscr{D} = \Omega \times \mathbb{R}$, where $\Omega \subset \mathbb{R}^2$ is the cross section. We assume a bounded cross section $\Omega = \Omega_B$ of the form

$$\Omega_B = \{[x, y] : x \in [0, b], y \in [h_{\mathrm{m}} + \beta(x), h_{\mathrm{M}}], \tag{21}$$

The heights $y = h_{\mathrm{m}}$ and $y = h_{\mathrm{M}}$ describe the minimum and maximum elevations of the fluid domain, respectively, with $h_{\mathrm{m}} < h_{\mathrm{M}}$, and $h_{\mathrm{m}} + \beta(x) \le h_{\mathrm{M}}$ for all x.

We will assume $\partial \mathscr{D} = \partial \Omega \times \mathbb{R} = \Gamma_{\mathrm{L}} \cup \Gamma_F \cup \Gamma_{\mathrm{B}}$, with Γ_{L} representing the lateral wall, Γ_F representing the free surface, and Γ_{B} the bottom,

$$\Gamma_{\mathrm{F}} = \{(x, h_{\mathrm{M}}, z) : z \in \mathbb{R}, 0 \le x \le b\}, \tag{22}$$
$$\Gamma_{\mathrm{B}} = \{(x, h_{\mathrm{m}} + \beta(x), z) : z \in \mathbb{R}, 0 \le x \le b\}, \tag{23}$$
$$\Gamma_{\mathrm{L}} = \{(0, y, z) : z \in \mathbb{R}, y \in [h_{\mathrm{m}} + \beta(0), h_{\mathrm{M}}]\} \cup \{(b, y, z) : $$
$$z \in \mathbb{R}, y \in [h_{\mathrm{m}} + \beta(b), h_{\mathrm{M}}]\}. \tag{24}$$

In this article we are interested in domains with $h_{\mathrm{m}} + \beta(x) = h_{\mathrm{M}}$ at $x = 0$ and $x = b$. Then $\Gamma_{\mathrm{L}} = \emptyset$.

To state the problem we introduce a velocity potential $\phi(x, y, z, t)$ and look for solutions of Laplace's equation

$$\phi_{xx} + \phi_{yy} + \phi_{zz} = 0 \text{ in } \mathscr{D}, \tag{25}$$

with

$$\begin{cases} \phi_t + g\eta = 0 \text{ at } \Gamma_F, \\ \eta_t = \phi_y \text{ at } \Gamma_F, \\ \frac{\partial \phi}{\partial \hat{n}} = 0 \text{ at } \Gamma_B \cup \Gamma_L, \end{cases} \tag{26}$$

see [33]. Equations (25), (26) are the linearized Euler equations for free surface potential flow.

We consider solutions of the following two forms:
A.

$$\phi(x, y, z, t) = \psi(x, y) \cos(\omega t), \tag{27}$$

referred to as *transverse modes*. see [14,28].
B.

$$\phi(x, y, z, t) = \psi(x, y) \cos(\kappa z - \omega t), \tag{28}$$

referred to as *longitudinal modes*, see [20,28].

We formulate the problem of finding solutions of the above form in terms of Dirichlet–Neumann operators.

We first consider transverse modes. Let the fluid domain consist of a straight channel and consider the case $\Omega = \Omega_B$. Consider $f : [0, b] \to \mathbb{R}$, and define the Dirichlet–Neumann operator G_0 by

$$(G_0 f)(x) = \frac{\partial \psi(x, y)}{\partial y}\Big|_{y=h_M}, \tag{29}$$

where $\psi : \Omega \to \mathbb{R}$ satisfies

$$\begin{cases} \Delta \psi = 0 \text{ in } \Omega, \\ \psi = f \text{ at } \Omega \cap \Gamma_F, \\ \frac{\partial \psi}{\partial \hat{n}} = 0 \text{ at } \Omega \cap (\Gamma_B \cup \Gamma_L), \end{cases} \tag{30}$$

Combining the first two equations of (26), the problem of finding transverse mode solutions (27) can be written as

$$G_0 f = g^{-1} \omega^2 f. \tag{31}$$

The classical (exact) approach to solving (25)–(27), or (29)–(31), is given in Sect. 4.1. We will compare the results to solutions of (31) with G_0 replaced by the

operators $\mathscr{A}_1(\beta)$, $\mathscr{A}_{G_0}(\beta)$, with depth topography as in (21), applied to $b-$periodic functions. We comment on this approximation at the end of this section.

We now consider longitudinal modes. Consider $f(x) = \psi(x, h_{\mathrm{M}})$, with $x \in [0, b]$, and define the modified Dirichlet–Neumann operator $G_{0,\kappa}$ by

$$(G_{0,\kappa} f)(x) = \frac{\partial \psi(x, y)}{\partial y}\Big|_{y = h_{\mathrm{M}}}, \tag{32}$$

where $\psi : \Omega \to \mathbb{R}$ satisfies

$$\begin{cases} \Delta \psi = \kappa^2 \psi \ \text{in} \ \Omega, \\ \psi = f \ \text{at} \ \Omega \cap \Gamma_{\mathrm{F}}, \\ \frac{\partial \psi}{\partial \hat{n}} = 0 \ \text{at} \ \Omega \cap (\Gamma_{\mathrm{B}} \cup \Gamma_{\mathrm{L}}), \end{cases} \tag{33}$$

with κ as in (28). By (25) and the first two equations of (26), the problem of finding longitudinal mode solutions (28) can be written as

$$G_{0,\kappa} f = g^{-1} \omega^2 f. \tag{34}$$

Comparing (25), (28), and the first equation of (33), $(G_{0,\kappa} f)(x)$ in (34) is the 3-D zeroth-order Dirichlet–Neumann operator, G_0 applied to functions $f(x) e^{\pm i\kappa z}$ (or $f(x) \cos(\kappa z)$).

The classical (exact) approach to solving (25)–(26) and (28), or (32)–(34), is given in Sect. 4.2. The solutions will be compared to solutions of (34) with $G_{0,\kappa}$ replaced by operators $\mathscr{A}_1$ of (19), $\mathscr{A}_{G_0}$ of (20), applied to functions of the form $e^{\pm i\kappa z} f(x)$, with f $b-$periodic. The depth topography is as in (21), and β is independent of z. Specifically, the operator $\mathscr{A}_1$ of (19) applied on functions of the form $e^{\pm i\kappa z} f(x)$ defines the operator $\mathscr{A}_{1,\kappa}(\beta)$ by

$$\begin{aligned}\mathscr{A}_{1,\kappa}(\beta) f = [\sqrt{D^2 + \kappa^2} \tanh(h_0 \sqrt{D^2 + \kappa^2}) \\ - \sqrt{D^2 + \kappa^2} \operatorname{sech}(h_0 \sqrt{D^2 + \kappa^2}) \beta(z) \sqrt{D^2 + \kappa^2} \operatorname{sech}(h_0 \sqrt{D^2 + \kappa^2})] f, \end{aligned} \tag{35}$$

with $h(x) = h_0 - \beta(x)$, $h_0 = h_{\mathrm{M}} - h_{\mathrm{m}} > 0$, and $D = -i\partial_x$. We will compute numerically the eigenmodes of $\mathscr{A}_{1,\kappa}(\beta)$ with $b-$periodic boundary conditions. Similarly, the ad-hoc operator $\mathscr{A}_{G_0}$ of (20) applied on functions of the form $e^{\pm i\kappa z} f(x)$ defines the operator $\mathscr{A}_{G_{0,\kappa}}(\beta)$ by

$$\mathscr{A}_{G_{0,\kappa}}(\beta) f = [Sym(\sqrt{D^2 + \kappa^2} \tanh(h(z) \sqrt{D^2 + \kappa^2}))] f, \tag{36}$$

with the notation of (35), and we will compute the eigenmodes of $\mathscr{A}_{G_{0,\kappa}}(\beta)$ with $b-$periodic boundary conditions. Symmetrization of operators on $b-$periodic functions is as in Sect. 2, using the standard inner product on real $b-$periodic L^2 functions.

Computations with $b-$periodic boundary conditions use the periodic analogues of the operators of Sect. 2 and above. In particular for a a real function and h, f real $b-$periodic functions, we let

$$[a(h(x)D)f](x) = \sum_{\lambda=-\infty}^{\infty} a(h(x)\lambda)\hat{f}_\lambda e^{i\lambda\frac{2\pi}{b}x}, \tag{37}$$

$$\hat{f}_\lambda = \frac{1}{b} \int_{-\frac{b}{2}}^{\frac{b}{2}} f(x)e^{-i\lambda\frac{2\pi}{b}x}\mathrm{d}. \tag{38}$$

Numerical computations use Galerkin truncations of the above operators to modes $|l| \leq l_{max}$. The discretization is described in Appendix A. We can simplify the calculations by noting that operators $\mathscr{A}_1$, $D\tanh(h(\cdot)D)$, $\mathscr{A}_2$ of Sect. 2 and $\mathscr{A}_{1,\kappa}(\beta)$, $\mathscr{A}_{G_{0,\kappa}}(\beta)$ above map real-valued functions to real-valued functions, and for β, h even they also preserve parity, see Appendix A. We can thus consider finite dimensional truncations of expansions in cosines and sines for the even and odd subspaces, respectively. The corresponding matrices are block-diagonal. In the case of $D\tanh(h(\cdot)D)$, we compute the matrix for $Sym(D\tanh(h(\cdot)D))$ by symmetrizing the truncation of $D\tanh(h(\cdot)D)$. Clearly, the adjoint (transpose) and symmetrization also preserve parity.

In the next section we describe some known semi-analytic solutions of the form (27), (28), obtained for some special domains with finite cross-section Ω and $\Gamma_L = \emptyset$, i.e. slopping beach geometries. These solutions are constructed starting with a multiparameter family of harmonic functions ϕ_μ of the form (27), or (28), defined on the plane and satisfying the rigid wall boundary condition on a set $\tilde{\Gamma}_B$ that includes Γ_B and is the boundary of a domain $\tilde{\mathscr{D}}$ that includes $\mathscr{D}$. Then we require that the ϕ_μ also satisfy the first two equations of (26) on the free surface Γ_F. This requirement leads to algebraic equations that restrict the allowed values of the parameter μ to a discrete set and also determine the frequencies. This construction does not assume any boundary conditions for the free surface potential.

The second computation in the next section computes $b-$periodic eigenfunctions of the approximate Dirichlet–Neumann operators defined in Sect. 2 and above, with $b-$periodic depth profiles with vanishing depth at integer multiples of $x = b$. Also, the domains we consider in the next section are symmetric in z so that the eigenfunctions of the approximate Dirichlet–Neumann operators are either even or odd, satisfying Neumann and Dirichlet boundary conditions, respectively, at $x = 0, b$.

4 Transverse and Longitudinal Modes in Triangular Cross-sections

Transverse and longitudinal modes can be calculated explicitly only for special geometries of the channel cross-sections. In this section we compare some exact results for triangular channels by Lamb [21] *Art. 261*, Macdonald [23], Greenhill [13], Packham [28], and Groves [14], to results obtained using the approximate Dirichlet–Neumann operators defined in the previous sections.
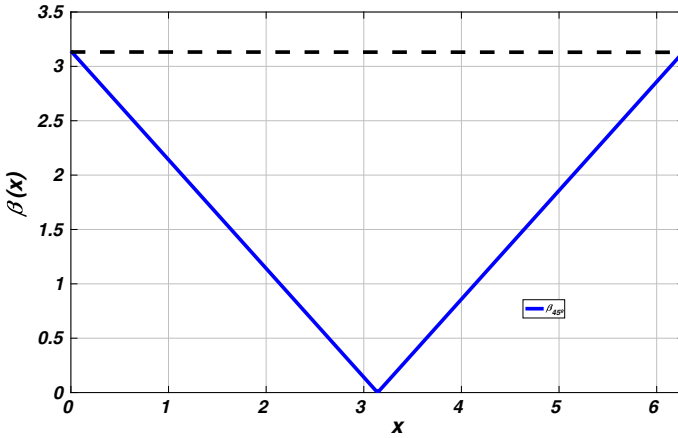
Fig. 3 Right isosceles triangular cross-section of a straight channel with the right angle at the bottom, see Eq. (39)

4.1 Transverse Modes for Triangular Cross-section: Right Isosceles Triangle

The first geometry we consider corresponds to a uniform straight channel with right isosceles triangle as a cross-section, see Fig. 3. The cross-section $\Omega = \Omega_B$ is as in (21) and the bottom is at $y = \beta_{45}(x)$. The minimum and maximum heights of the the fluid domain are $h_m = 0$ and $h_M = \pi$, respectively. The channel width is $b = 2\pi$, and

$$\beta_{45}(x) = \begin{cases} -x + \pi & \text{in } 0 \le x < \pi \\ x - \pi & \text{in } \pi \le x \le 2\pi. \end{cases} \tag{39}$$

Normal modes for this channel were obtained by Kirchhoff, see Lamb [21], *Art. 261*, and include symmetric and antisymmetric modes. The symmetric transverse modes, see (27), are given by potentials $\phi(x, y, z, t) = \psi(x, y)\cos(\omega t)$ with

$$\psi(x, y) = A[\cosh(\alpha(x - \pi))\cos(\beta y) + \cos(\beta(x - \pi))\cosh(\alpha y)]. \tag{40}$$

It can be checked that $\frac{\partial \phi}{\partial y}\big|_{y=h_M}$ and ϕ are symmetric with respect to the $x = \pi$ axis. Also ϕ satisfies the rigid wall boundary condition

$$\frac{\partial \phi}{\partial \hat{n}} = 0 \quad \text{at} \quad y = |x - \pi|. \tag{41}$$

To impose the boundary condition at the free surface $y = h_M$, we use the first two equations of (26) to obtain

$$\omega^2 \psi = g\frac{\partial \psi}{\partial y} \quad \text{at} \quad y = h_M. \tag{42}$$

Combining the requirement $\Delta\psi = 0$ with (40) we have the conditions

$$\alpha^2 - \beta^2 = 0, \tag{43}$$

and

$$\omega^2 \cosh(\alpha h_M) = -g\alpha \sinh(\alpha h_M), \quad \omega^2 \cos(\beta h_M) = g\beta \sin(\beta h_M) = 0, \tag{44}$$

or equivalently

$$\alpha h_M \tanh(\alpha h_M) + \beta h_M \tan(\beta h_M) = 0. \tag{45}$$

The values of α, β are determined by the intersections of the curves (43) and (45), see Fig. 4. There is an infinite number of solutions, $h_M\alpha_i$, $i = 0, 2, 4, \ldots$, with $\alpha_i < \alpha_{i'}$ if $i < i'$. The corresponding frequencies ω_i are obtained by (44). The first values of $h_M\alpha_i$, ω_i are shown in Table 1.

To obtain the antisymmetric modes we use the potentials $\phi(x, y, z, t) = \psi(x, y) \cos(\omega t)$ with

$$\psi(x, y) = B[\sinh(\alpha(x - \pi)) \sin(\beta y) + \sin(\beta(x - \pi)) \sinh(\alpha y)]. \tag{46}$$

We check that ϕ satisfies the rigid wall boundary conditions at $y = |x - \pi|$. We also check that $\frac{\partial\phi}{\partial y}|_{y=h_M}$ is antisymmetric with respect to the $x = 0$ axis. Imposing the free surface boundary conditions (26) to (27) we obtain (42). Then $\Delta\psi = 0$ and (46) lead to the conditions

$$\alpha^2 - \beta^2 = 0 \tag{47}$$

and

$$\omega^2 \sinh(\alpha h_M) = g\alpha \cosh(\alpha h_M), \quad \omega^2 \sin(\beta h_M) = g\beta \cos(\beta h_M), \tag{48}$$

or

$$\alpha h \coth(\alpha h_M) = \beta h_M \cot(\beta h_M). \tag{49}$$

The values of α, β are determined by the intersections of the curves (47) and (49), see Fig. 5. There is an infinite number of solutions $h_M\alpha_i$, $i = 1, 3, 5\ldots$ with $\alpha_i < \alpha_{i'}$ if $i < i'$. The corresponding frequencies ω_i are given by (48), see Table 1.

By the first two equations of (26), and the form of ϕ, the free surface corresponding to the above symmetric and antisymmetric satisfies

$$\eta(x, y, t) = -\frac{1}{g}\omega\psi(x, y)|_{y=h_M} \sin\omega t = \frac{1}{\omega}\frac{\partial\psi(x, y)}{\partial y}|_{y=h_M} \sin\omega t. \tag{50}$$

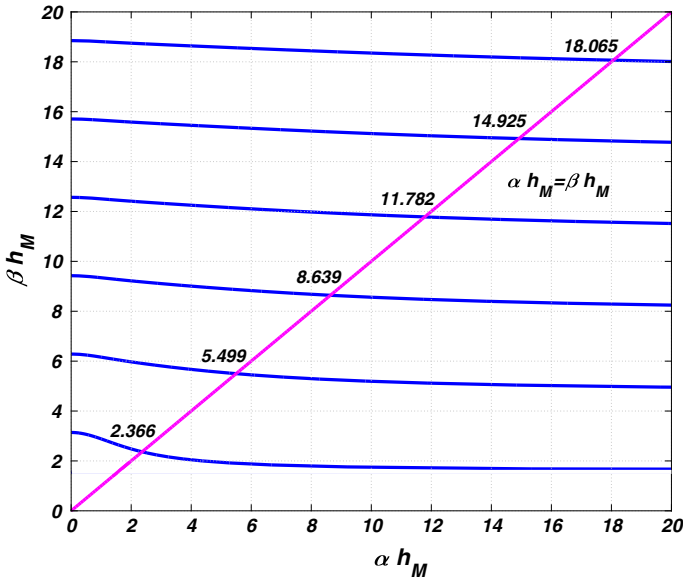The amplitude of η is, therefore, $\omega^{-1}\frac{\partial\psi(x,y)}{\partial y}|_{y=h_M}$.

Fig. 4 Even modes. Intersection of curves (43) and (45)

Table 1 Frequencies of modes for channel of Fig. 3 these values are associated with graphic roots in Figs. 4 and 5

	$i = 0$	$i = 1$	$i = 2$	$i = 3$	$i = 4$	$i = 5$	$\cdots$
$\alpha_i h_{\mathrm{M}}$	2.365	3.927	5.499	7.068	8.639	10.210	$\cdots$
ω_i	2.6923	3.4986	4.1416	4.6955	5.1912	5.6435	$\cdots$

We use $h_{\mathrm{M}} = \pi$. Notice that i corresponds to the mode number

In Fig. 6 we compare the surface amplitude of the exact symmetric and antisymmetric modes found above to the surface amplitudes obtained by computing numerically the eigenfunctions of the approximate Dirichlet–Neumann operators $\mathscr{A}_{G_0}(\beta_{45°})$ of (15), and $\mathscr{A}_1(\beta_{45°})$ with 2π−periodic boundary conditions. The surface amplitude η is obtained by $\eta = \omega^{-1}\mathscr{A}(\beta)f$, with $\mathscr{A}(\beta)$ representing each of the two approximate Dirichlet–Neumann operators. This expression is analogous to (50).

Figure 6 suggests good quantitative agreement between the exact even modes and the even modes obtained by $\mathscr{A}_{G_0}, \mathscr{A}_1(\beta)$, with some discrepancy near the boundary for the first mode. The $\mathscr{A}_{G_0}$ modes seem closer to the exact ones in the interior. For the odd modes, the two approximate operators lead to vanishing amplitude at the boundary. This is a consequence of the parity considerations of the previous section. On the other hand, exact odd modes have non-vanishing values at the boundary, in fact they appear to have local extrema at the boundary. This leads to a discrepancy between exact and approximate modes at the boundary. The first two modes of $\mathscr{A}_{G_0}, \mathscr{A}_1(\beta)$ and of the exact approach differ quite significantly also in the interior of the domain, with the $\mathscr{A}_{G_0}$ modes being somewhat closer to the exact ones. For higher modes, the
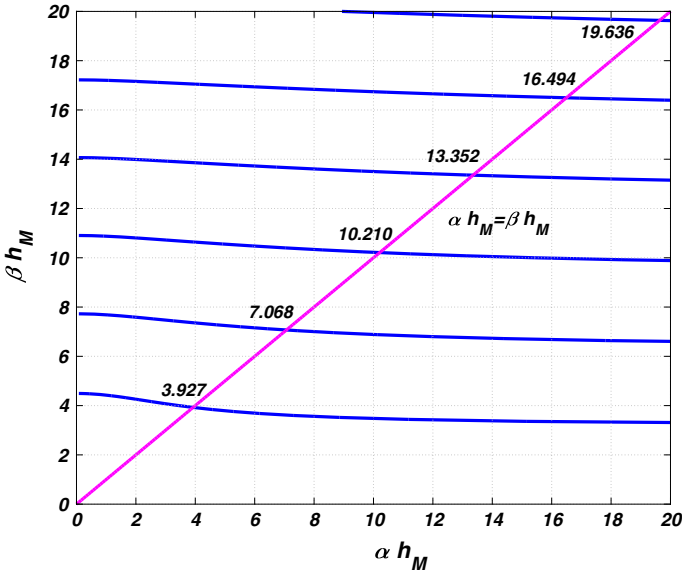
Fig. 5 Odd modes. Intersection of curves (47) and (49)

discrepancy at the boundary persists, but the values of the interior are close for all four sets of modes.

Tables 2, 3, 4, 5 show the L^2 distance between the exact modes and the numerical modes $\mathscr{A}_{G_0}$, $\mathscr{A}_1(\beta)$ of Fig. 6 computed using different spatial resolutions. We considered spectral truncations with $K = 2^4$ to 2^9 Fourier cosine/sine modes for even/odd modes, respectively, and see evidence for convergence as the resolution increases. The value $K = 2^6$ used in Fig. 6 and the figures below is seen to capture the behavior seen using higher resolution. The tables indicate clearly the better approximation of the even modes, and we see that the L^2 difference between the exact even modes and the even $\mathscr{A}_{G_0}$ modes is about half of the L^2 difference between the exact even modes and the even $\mathscr{A}_1(\beta)$ modes.

The procedure for obtaining the exact modes does not require any conditions on the value of the potential at the intersection of the free boundary and the rigid wall. Also, the free surface is described by a value of the $y-$coordinate, and this allows us to define $\eta(z)$ for all real x; in particular, we determine the fluid domain by computing the intersection of the graph of η with the rigid wall (Fig. 6 only shows $\eta(x)$, $x \in [0, 2\pi)$). The exact approach leads then to a more realistic motion of the surface at the sloping beach. This does not imply that the exact solutions are physical either, since the boundary conditions at the free surface are not exact. In contrast, the odd modes of the approximate operators correspond to pinned boundary conditions that are not expected to be physical.

We have also used the approximate operators $\mathscr{A}_{G_0}$ and $\mathscr{A}_1$ to compute the $2\pi-$periodic normal modes for domains obtained from the triangular channel β_{45} by adding a fluid layer of depth T, see Fig. 7. Thus the minimum and maximum heights of the domain are at $h_m = 0$ and $h_M = \pi + T$, respectively, and the bottom at each

Table 2 L^2 difference between exact even modes and numerical even modes of $\mathscr{A}_{G_0}(\beta_{45})$, truncation with K Fourier-cosine modes

Even modes	$K = 2^4$	2^5	2^6	2^7	2^8	2^9
$\|\eta - \eta_{\mathscr{A}_{G_0}}\|_{L^2}$ for even modes, K cosine modes						
$0 - Mode$	0.0720	0.0530	0.0354	0.0298	0.0286	0.0283
$2 - Mode$	0.1167	0.0731	0.0581	0.0538	0.0519	0.0509
$4 - Mode$	0.1069	0.0799	0.0789	0.0787	0.0792	0.0792
$6 - Mode$	0.1922	0.0864	0.0689	0.0679	0.0662	0.0649
$8 - Mode$	0.1958	0.0834	0.0772	0.0821	0.0819	0.0807

Table 3 L^2 difference between exact odd modes and numerical odd modes of $\mathscr{A}_{G_0}(\beta_{45})$, truncation with K Fourier-sine modes

Odd modes	$K = 2^4$	2^5	2^6	2^7	2^8	2^9
$\|\eta - \eta_{\mathscr{A}_{G_0}}\|_{L^2}$ for odd modes, K sine modes						
$1 - Mode$	0.6475	0.6124	0.5908	0.5804	0.5756	0.5333
$3 - Mode$	0.5285	0.4960	0.4766	0.4673	0.4630	0.4610
$5 - Mode$	0.5424	0.4914	0.4650	0.4525	0.4468	0.4442
$7 - Mode$	0.6111	0.5086	0.4739	0.4579	0.4505	0.4471
$9 - Mode$	0.6302	0.5296	0.4688	0.4677	0.4590	0.4549

Table 4 L^2 difference between exact even modes and numerical even modes of $\mathscr{A}_1(\beta_{45})$, truncation with K Fourier-cosine modes

Even modes	$K = 2^4$	2^5	2^6	2^7	2^8	2^9
$\|\eta - \eta_{\mathscr{A}_1}\|_{L^2}$ for even modes, K cosine modes						
$0 - Mode$	0.1486	0.1305	0.1208	0.1163	0.1141	0.1129
$2 - Mode$	0.2258	0.2040	0.1944	0.1901	0.1881	0.1871
$4 - Mode$	0.4455	0.4006	0.3768	0.3645	0.3583	0.3552
$6 - Mode$	0.4756	0.4158	0.3845	0.3685	0.3605	0.3564
$8 - Mode$	0.5270	0.4381	0.4007	0.3818	0.3724	0.3677

$x = [0, 2\pi]$ is at $-h(x) = -T - \pi + \beta_{45}(x)$, with β_{45} as in (39), and $T \geq 0$. We then define $\mathscr{A}_{G_0}(\beta_{45}, T)$ by the right-hand side of (15) with $h(x) = T + \pi - \beta_{45}(x)$, and $\mathscr{A}_1(\beta, T)$ by the right-hand side of (14) with $h_0 = T + \pi$, and $\beta = \beta_{45}(x)$, and examine their 2π−periodic normal modes as $T \to 0$. In both cases we see convergence to the $T = 0$ modes computed above. We indicate this in Fig. 8 and Table 6 where we show the first four odd and even modes of $\mathscr{A}_{G_0}(\beta_{45}, T)$ for three values of T. Similar results were obtained for $\mathscr{A}_{1,T}$. Also, even modes satisfy a Neumann boundary condition at $x = 0, 2\pi$, and the interval of length T can be interpreted also as the height of a vertical wall at $x = 0, 2\pi$.

Table 5 L^2 difference between exact odd modes and numerical odd modes of $\mathscr{A}_1(\beta_{45})$, truncation with K Fourier-sine modes

Odd modes	$K = 2^4$	2^5	2^6	2^7	2^8	2^9
$\|\eta - \eta_{\mathscr{A}_1}\|_{L^2}$ for odd-modes, K sine modes						
$1 - Mode$	0.5632	0.5268	0.5077	0.4978	0.4928	0.4903
$3 - Mode$	0.4441	0.4120	0.3949	0.3861	0.3816	0.3794
$5 - Mode$	0.4455	0.4006	0.3768	0.3645	0.3583	0.3552
$7 - Mode$	0.4756	0.4158	0.3845	0.3685	0.3605	0.3564
$9 - Mode$	0.5499	0.4381	0.4007	0.3818	0.3724	0.3677

Convergence to the triangular domain modes as $T \to 0$ indicates more clearly that normal modes of the approximate $2\pi-$periodic operators used for a triangular domain are limiting cases of operators defined for a $2\pi-$periodic depth profile with depth that does not vanish anywhere. In that case the definition and computations of the Dirichlet–Neumann operator follow the construction of [7], but cannot take into account the sloping beach boundary. Note also that the $2\pi-$periodic modes obtained using the $2\pi-$periodic $\mathscr{A}_{G_0}(\beta_{30°})$, $\mathscr{A}_1(\beta_{30°})$, are special cases of the Floquet–Bloch modes for the $2\pi-$periodic depth profile, see [9] for a study of the the band structure and Floquet–Bloch modes of $\mathscr{A}_1(\beta)$ with another periodic profile.

The above experiments were performed with larger T, and with an alternative set of depth profiles where the minimum and maximum heights of the domain are at $h_m = 0$ and $h_M = \pi$ and $\beta(x) = |\sigma(x - \pi)|$, with σ varying in $[0, 1]$, i.e. decreasing σ we approach the constant depth case. Increasing T and decreasing σ is expected to make $\mathscr{A}_1$ a more accurate approximation of the Dirichlet–NeumannDirichlet–Neumann operator in the respective domains. We have seen that the normal modes of $\mathscr{A}_1$ change little as we vary T or σ away from the $T = 0$, $\sigma = 1$, respectively, suggesting that $\mathscr{A}_1$ is already a reasonable approximation for the small $T > 0$ periodic depth profile, despite the fact that β is the order of the maximum depth. This is likely due to the fact that $h_0 = \pi$ is already a value that makes the variable depth part of $\mathscr{A}_1$ a relatively small correction. Figure 6 suggests that the modes of $\mathscr{A}_{G_0}$ and $\mathscr{A}_1$ are close for $T = 0$, $\sigma = 1$, and their L^2 difference is seen to be ~ 0.4 or smaller. As T is increased and σ decreased this distance decreases. This suggests that $\mathscr{A}_{G_0}$ is also a reasonable approximation of the Dirichlet–Neumann operator for the small $T > 0$ depth profile.

4.2 Longitudinal Modes for Triangular Cross-sections: isosceles Triangle with Unequal Angle of 120°

A second geometry with exact longitudinal modes was considered by Macdonald [23], Packham, [28], see also Lamb [21], *Art. 261*. This geometry corresponds to a uniform straight channel with isosceles triangle cross-section with a unequal angle at the bottom of 120°, as illustrated in Fig. 9. In this case we will examine longitudinal modes.
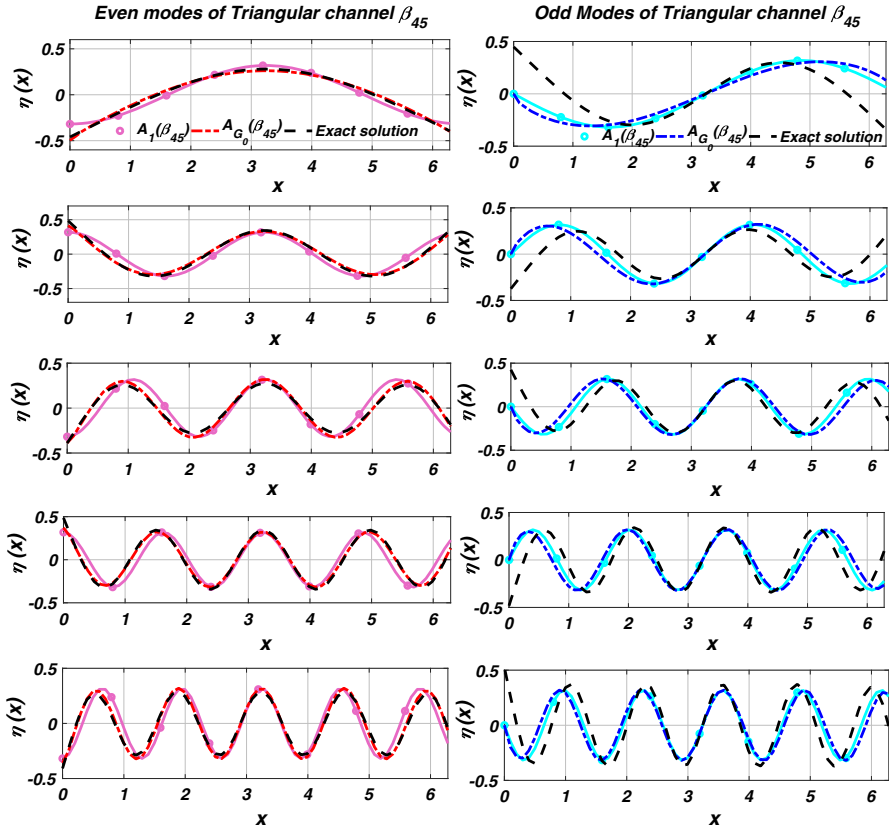
Fig. 6 Transverse modes of a channel with isosceles triangular cross-section illustrated in Fig. 3. Spectral truncation with $K = 2^6$ cosine/sine modes for even/odd modes. Left: even modes. Pink (circle-line): operator $\mathscr{A}_1(\beta_{45})$. Red (dot-dashed-line): operator $\mathscr{A}_{G_0}(\beta_{45})$. Black (dashed lines): exact solutions given by (40) and the values in Table 1. Right: odd modes. Cyan (circle-line): operator $\mathscr{A}_1(\beta_{45})$. Blue (dot-dashed-line): operator $\mathscr{A}_{G_0}(\beta_{45})$. Black (dashed lines): exact solutions given by (46) and the values in Table 1 (color figure online)

We consider the cross-section $\Omega = \Omega_B$, as in (21) and the bottom $\beta_{30}(x)$ of (51). The channel width is $b = 2\pi$ and the maximum and minimum heights of the fluid domain are $h_M = \frac{\pi}{\sqrt{3}}$ and $h_m = 0$, respectively. The cross-section profile is given by

$$\beta_{30}(x) = \begin{cases} \frac{-1}{\sqrt{3}}x + \frac{\pi}{\sqrt{3}}, & 0 \leq x < \pi \\ \frac{1}{\sqrt{3}}x - \frac{\pi}{\sqrt{3}}, & \pi \leq x \leq 2\pi \end{cases}, x \in [0, 2\pi]. \tag{51}$$

The exact solutions for symmetric modes, see Packham [28], and Groves [14] are as follows.
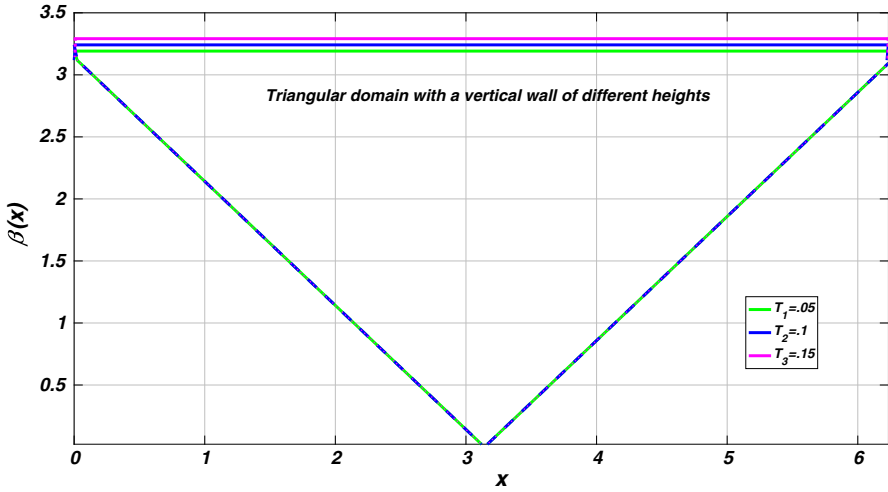
Fig. 7 Cross section of the straight channels with lateral boundary Γ_L. Vertical walls of heights $T_1 = 0.05$ (green), $T_2 = 0.1$ (blue), $T_3 = 0.15$ (magenta) (color figure online)
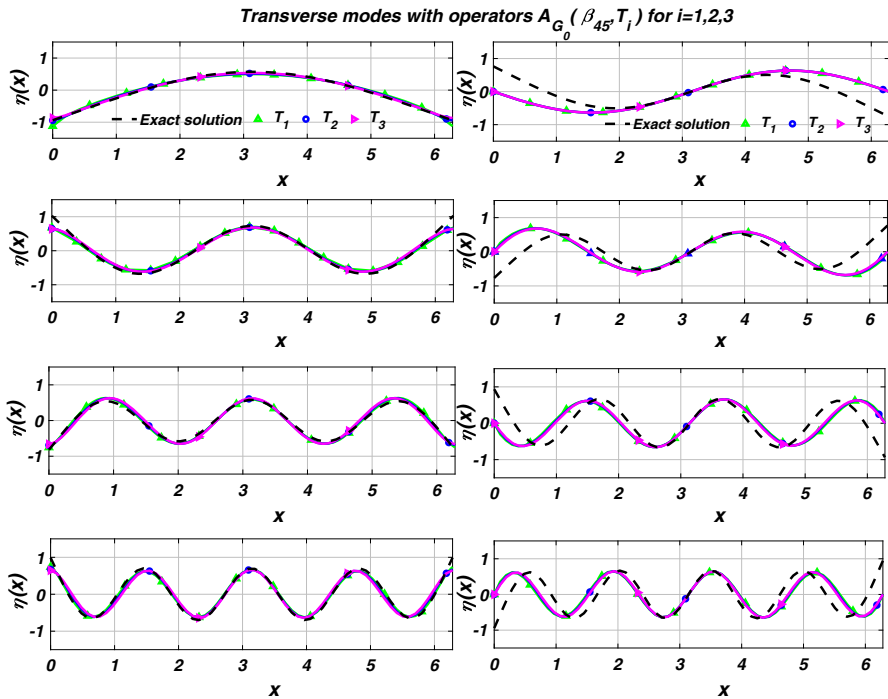

Fig. 8 Transverse modes with $\mathscr{A}_{G_0}(\beta_{45}, T_j)$ for the three cross sections of Fig. 7, vertical walls of heights $T_1 = 0.05$ (green upward-pointing triangle-line), $T_2 = 0.1$ (blue circle-line), $T_3 = 0.15$ (magenta right-pointing triangle-line). Even/odd modes computed using $K = 2^6$ Fourier sine/cosine modes (color figure online)

Table 6 L^2 difference between modes of $\mathscr{A}_{G_0}$ and $\mathscr{A}_{G_0(\beta_{45},T_j)}$, T_j, $j = 1, 2, 3$ as in Fig. 8, $K = 2^6$ Fourier sine/cosine modes. Notice that i corresponds to the mode number

L^2 difference, modes of $\mathscr{A}_{G_0(\beta_{45},T)}$, $T = 0$, $T = T_j$, $j = 1, 2, 3$, Fig. 8								
	$i = 0$	$i = 1$	$i = 2$	$i = 3$	$i = 4$	$i = 5$	$i = 6$	$i = 7$
$\\|\eta_{\mathscr{A}_{G_0(\beta_{45},0)}} - \eta_{\mathscr{A}_{G_0(\beta_{45},T_3)}}\\|_{L^2}$	0.0181	0.0141	0.0408	0.0362	0.0660	0.0619	0.0844	0.0847
$\\|\eta_{\mathscr{A}_{G_0(\beta_{45},0)}} - \eta_{\mathscr{A}_{G_0(\beta_{45},T_2)}}\\|_{L^2}$	0.0132	0.0105	0.0303	0.0273	0.0502	0.0475	0.0660	0.0667
$\\|\eta_{\mathscr{A}_{G_0(\beta_{45},0)}} - \eta_{\mathscr{A}_{G_0(\beta_{45},T_1)}}\\|_{L^2}$	0.0073	0.0059	0.0172	0.0157	0.0291	0.0279	0.0393	0.0402
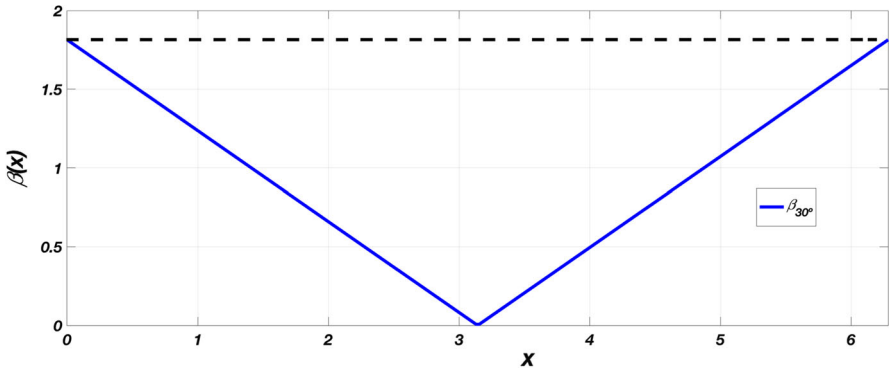
Fig. 9 Straight channel with isosceles triangular cross-section with the unequal angle at the bottom of $120°$, see (51)

The $0-$mode is described by a velocity potential ϕ of the form (28) with

$$\psi(x, y) = A \left[\cosh(\kappa(y - h_M)) + \frac{\omega^2 \kappa^2}{g\kappa} \sinh(\kappa(y - h_M)) \right.$$
$$+ 2 \cosh \left(\frac{\sqrt{3}\kappa(x - \pi)}{2} \right)$$
$$\left. \times \left\{ \cosh \left(\kappa \left(\frac{y}{2} + h_M \right) \right) - \frac{\omega^2 \kappa^2}{g\kappa} \sinh \left(\kappa \left(\frac{y}{2} + h_M \right) \right) \right\} \right], \quad (52)$$

and

$$\omega^2 = \frac{3g}{4\kappa} \coth \left(\frac{3\kappa h_M}{2} \right) \left\{ 1 + \left(1 - \frac{8}{9} \tanh^2 \left(\frac{3\kappa h_M}{2} \right) \right)^{\frac{1}{2}} \right\}. \quad (53)$$

The remaining symmetric modes 2, 4, 6, 8, ... are described by a velocity potential ϕ of the form (28) with

$$
\psi(x, y) = A\left[\left\{\cosh(\alpha(y - h_M)) + \frac{\omega^2 \kappa^2}{g\kappa} \sinh(\alpha(y - h_M))\right\} \cos(\beta(x - \pi))\right.
$$

$$
+ 2\cosh\left(\frac{\sqrt{3}\alpha(x - \pi)}{2}\right) \cos\left(\frac{\sqrt{3}\beta y}{2}\right) \cos\left(\frac{\beta(x - \pi)}{2}\right)
$$

$$
\times \left\{\cosh\left(\alpha\left(\frac{y}{2} + h_M\right)\right) - \frac{\omega^2 \kappa^2}{g\kappa} \sinh\left(\alpha\left(\frac{y}{2} + h_M\right)\right)\right\}
$$

$$
- 2\sinh\left(\frac{\sqrt{3}\alpha(x - \pi)}{2}\right) \sin\left(\frac{\sqrt{3}\beta y}{2}\right) \sin\left(\frac{\beta(x - \pi)}{2}\right)
$$

$$
\left. \times \left\{\sinh\left(\alpha\left(\frac{y}{2} + h_M\right)\right) - \frac{\omega^2 \kappa^2}{g\kappa} \cosh\left(\alpha\left(\frac{y}{2} + h_M\right)\right)\right\}\right], \tag{54}
$$

and

$$
\omega^2 = \frac{g\alpha}{\kappa^2}\left[\frac{\frac{\beta}{\alpha}\sqrt{3}(\cosh(3\alpha h_M) - \cos(\sqrt{3}\beta h_M))}{\frac{\beta}{\alpha}\sqrt{3}\sinh(3\alpha h_M) - 3\sin(\sqrt{3}\beta h_M)}\right]. \tag{55}
$$

The above potentials are harmonic and satisfy the rigid wall boundary conditions.

The first two equations of motion of (26), (28), and (54) lead to

$$
\alpha^2 - \beta^2 = \kappa^2, \tag{56}
$$

and

$$
\left(\frac{\beta}{\alpha}\right)^2 \cosh(3\alpha h_M) \cos(\sqrt{3}\beta h_M)
$$

$$
- \frac{1}{4}\left(\frac{\beta}{\alpha}\right)\sqrt{3}\left\{1 - \left(\frac{\beta}{\alpha}\right)^2\right\} \sinh(3\alpha h_M) \sin(\sqrt{3}\beta h_M)
$$

$$
- \frac{1}{4}\left[\left\{3 + 5\left(\frac{\beta}{\alpha}\right)^2\right\} - \left\{3 + \left(\frac{\beta}{\alpha}\right)^2\right\} \cos^2(\sqrt{3}\beta h_M)\right] = 0. \tag{57}
$$

In Figs. 10, 11 we show the symmetric longitudinal modes derived with the values of α and β obtained from relations (56) and (57) for $\kappa = 2$, see also Table 7.

By the first two equations of (26) and (28), the free surface corresponding to the above modes can be computed by

$$
\eta(x, t) = -\frac{1}{\omega}\frac{\partial \psi(x, y)}{\partial y}\Big|_{y = h_M} \sin \omega t. \tag{58}
$$

The amplitude of η is, therefore, $\omega^{-1}\frac{\partial \psi(x, y)}{\partial y}\Big|_{y = h_M}$.
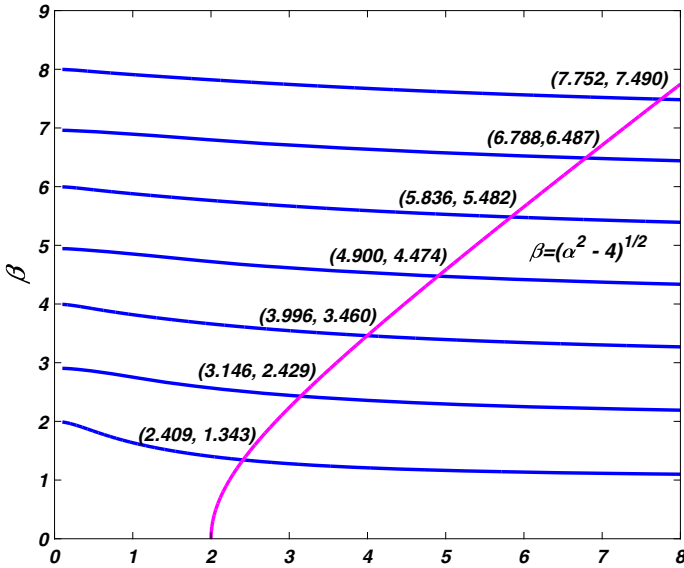
Fig. 10 Graphs for the determination of α and β for the modes 2, 4, 6, 8, and 10 using $\kappa = 2$, $h_M = \frac{\pi}{\sqrt{3}}$

**Table 7** Frequencies of modes of channel of Fig. 9; these values are associated with graphic roots in Fig. 10

	$i = 2$	$i = 4$	$i = 6$	$i = 8$	$i = 10$	$\cdots$
α_i	2.409	3.146	3.996	4.900	5.836	$\cdots$
β_i	1.343	2.429	3.460	4.474	5.482	$\cdots$
ω_i	2.4297	2.7764	3.1289	3.4651	3.7813	$\cdots$

We use $h_M = \frac{\pi}{\sqrt{3}}$. Notice that i corresponds to the mode number

In Fig. 11 we compare the surface amplitude of the exact symmetric modes to the surface amplitudes obtained by computing numerically the eigenfunctions of the approximate Dirichlet–Neumann operators $\mathscr{A}_{G_{0,\kappa}}(\beta)$, $\mathscr{A}_{1,\kappa}(\beta)$ of (36), (35), respectively, with β as in (51). We use $\kappa = 2$. To compute the eigenfunctions of $\mathscr{A}_{G_{0,\kappa}}(\beta)$, $\mathscr{A}_{1,\kappa}(\beta)$ numerically we use 2π−periodic boundary conditions. Also, given a computed eigenfunction f of $\mathscr{A} = \mathscr{A}_{G_{0,\kappa}}(\beta)$ or $\mathscr{A}_{1,\kappa}(\beta)$ the surface amplitude η is given by $\eta = \omega^{-1}\mathscr{A}$. This is analogous to (58).

In Fig. 11 we see some discrepancies between the first exact even mode and the first even $\mathscr{A}_{G_{0,\kappa}}(\beta)$ mode. For higher even modes, the $\mathscr{A}_{G_{0,\kappa}}(\beta)$ modes are close to the exact modes in the interior, but show discrepancies at the boundary. Also the even modes obtained by $\mathscr{A}_{G_{0,\kappa}}(\beta)$, $\mathscr{A}_{1,\kappa}(\beta)$ are generally close both in the interior and the boundary, with more pronounced discrepancies for the first and second modes. This fact is also illustrated in Table 8.

To our knowledge there are no exact solutions reported in the literature for odd modes. Odd modes obtained with the approximate Dirichlet-Neumann operators $\mathscr{A}_{G_{0,\kappa}}(\beta_{30})$, $\mathscr{A}_{1,\kappa}(\beta_{30})$ are shown in Fig. 11.
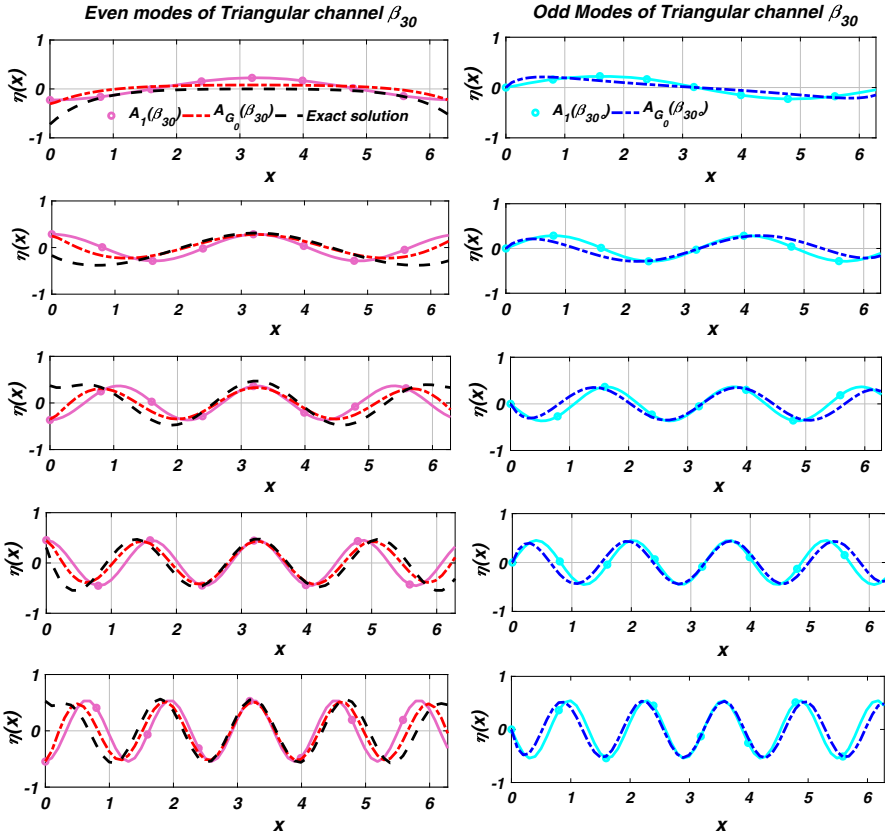
Fig. 11 Longitudinal modes of a channel with isosceles triangular cross-section illustrated in Fig. 9. The x-grid size is $K = 2^6$. Left: even modes with $\kappa = 2$. Pink (circle-line): operator $\mathscr{A}_1(\beta_{30})$. Red (dot-dashed-line): operator $\mathscr{A}_{G_0}(\beta_{30})$. Black (dashed lines): exact solutions given by (54) and (55) and the values in Table 7. Right: odd modes with $\kappa = 2$. Cyan (circle-line): operator $\mathscr{A}_1(\beta_{30})$ with $\kappa = 2$. Blue (dot-dashed-line): operator $\mathscr{A}_{G_0}(\beta_{30})$ (color figure online)

Table 8 L^2 norm between the exact $i - th$ (even) exact mode and the corresponding evenmodes computed using. $\mathscr{A}_1(\beta_{30})$, $\mathscr{A}_{G_0}(\beta_{30})$, spectral truncations with $K = 2^6$ cosine modes. Notice that i corresponds to the mode number

$\|\|\|_{L^2}$ error between exact and numerical even-mode solutions in Fig. 11						
	$i = 0$	$i = 2$	$i = 4$	$i = 6$	$i = 8$	$\cdots$
$\mathscr{A}_1(\beta_{30})$	0.3988	0.7009	0.7238	0.7444	0.9474	$\cdots$
$\mathscr{A}_{G_0}(\beta_{30})$	0.7173	0.4408	0.4421	0.3801	0.5935	$\cdots$

5 Discussion

We have studied linear water wave modes in channels with variable depth, choosing depth geometries and models with known exact results. The main goal was to test

simplifications of the variable depth Dirichlet–Neumann operator for variable depth. We considered the lowest order Dirichlet–Neumann operator $\mathscr{A}_1$ in the depth variation expansion of Craig, Guyenne, Nicholls and Sulem [6], and an ad-hoc operator $\mathscr{A}_{G_0}$ of [32]. The exact results involve slopping beach geometries, while the approximate Dirichlet–Neumann operators we use are seen to be limits of approximate Dirichlet–Neumann operators for periodic topographies with nowhere vanishing depth. This observation suggests that the problems we compare are not equivalent. Despite this fact, we see reasonable agreement in the interior of the domain, with most discrepancies at the boundary of the free surface.

In the case of 2-D even modes the approximate operators yield good approximations of the exact modes even at the boundary. In the case of 2-D odd modes, the approximate Dirichlet–Neumann operators impose Dirichlet boundary conditions and miss the boundary behavior of the exact modes. In general, the exact modes seem to have local extrema at the boundary, and this may explain why the even modes of the periodic approximate Dirichlet–Neumann operators may give a better fit. We also think that Neumann boundary conditions, allowing odd modes, may give better approximations. In the case of 3-D longitudinal waves, the exact approach only yields even modes. The approximate operators give reasonable approximations of the exact modes in the interior of the domain, but can miss the boundary behavior. We suspect that Neumann boundary conditions may also be more appropriate. Also, the modes of $\mathscr{A}_{G_0}$ are somewhat closer to the exact modes than the $\mathscr{A}_1$ modes in the L^2 sense, by about a factor of a half. The results for the two approximate operators are, therefore, close, even though $\mathscr{A}_1$ is of first order in the depth variation β while $\mathscr{A}_{G_0}$ is of $O(1)$ in β. It seems possible that higher order terms in the depth expansion of [6] can improve the approximation away from the boundary. We also provide evidence that in the β_{45} geometry $\mathscr{A}_1$ and $\mathscr{A}_{G_0}$ are reasonable approximations of the Dirichlet–Neumann operator for nearby depth topographies with small minimum depth. Vanishing depth leads to nearby normal modes; we, therefore, think that the differences with the exact modes are mainly due to the different boundary conditions.

While the motivation of this work was to examine the accuracy of simple approximations of the Dirichlet–Neumann operator for general topographies, a possible question for further work is the usefulness of non-vanishing depth Dirichlet–Neumann operators to problems with slopping beach geometries. The fact that the Dirichlet–Neumann operator is known semi-analytically for some special domains with sloping beach domains can lead to more precise comparisons to approximate operators obtained under non-vanishing depth assumptions such as the ones considered in the present study, and to a theoretical understanding of the interior and boundary behavior.

Appendix A

We present some computations related to symmetrization, parity, and the operator $D \tanh(h(\cdot)D)$.

The notion of adjoint $\mathscr{A}^*$ applies to operators $\mathscr{A} : D(\mathscr{A}) \subset L^2 \to L^2$, with $D(\mathscr{A})$ dense in $L^2 = L^2(\mathbb{R}; \mathbb{R})$. Operators that map real-valued functions to real-valued (resp. imaginary-valued) functions will be denoted as *real* (resp. *imaginary*) operators. Imaginary operators map $D(\mathscr{A}) \subset L^2$ to iL^2. The adjoint and symmetrization of a real operator is real. We extend the definition of the adjoint to imaginary operators by linearity: if $\mathscr{A}$ is imaginary, then $\mathscr{B} = i\mathscr{A}$ is real and $\mathscr{A} = -i\mathscr{B}$ and we let $\mathscr{A}^* = -i\mathscr{B}^*$. We note that D and $\tanh(h(x)D)f$ are imaginary, and, therefore, $D \tanh(h(x)D)f$ is real. Similarly, we check that operators $\mathscr{A}_1, \mathscr{A}_2, \mathscr{A}_{1,\kappa}(\beta), \mathscr{A}_{G_{0,\kappa}}(\beta)$ are also real.

Also, for β, h even we check that $\mathscr{A}_1, \mathscr{A}_2, D \tanh(h(x)D), \mathscr{A}_{1,\kappa}(\beta)$, and $\mathscr{A}_{G_{0,\kappa}}(\beta)$ preserve parity, i.e. map even (resp. odd) real-valued functions to even (resp. odd) real-valued functions. This follows by examining the various operators appearing in the, respective. definitions and their compositions.

For instance, the operator D maps even (resp. odd) real-valued functions to odd (resp. even) imaginary-valued functions. Also, by the definition of $\tanh(h(x)D)$ on the line,

$$
\begin{aligned}
g_1(x) &= \tanh(h(x)D) \cos kx = \frac{1}{2}[\tanh(h(x)k)e^{ikx} + \tanh(h(x)(-k)e^{-ikx}] \\
&= i \tanh(h(x)k) \sin kx, \\
g_2(x) &= \tanh(h(x)D) \sin kx = \frac{1}{2i}[\tanh(h(x)k)e^{ikx} - \tanh(h(x)(-k))e^{-ikx}] \\
&= -i \tanh(h(x)k) \cos kx.
\end{aligned}
$$

Then h even implies $g_1(-x) = -g_1(x)$, and $g_2(-x) = g_2(x)$, for all x. Therefore, $\tanh(h(x)D)$ maps even (resp. odd) real-valued functions to odd (resp. even) imaginary-valued functions, and $D \tanh(h(x)D)$ is real and preserves parity Similar calculations apply to $b-$periodic functions, e.g. with k integer if $b = 2\pi$. Operators $\mathscr{A}_{1,\kappa}(\beta)$ of (35) and $\mathscr{A}_{G_{0,\kappa}}(\beta)$ of (36) are compositions of real operators that preserve parity.

We use the above observations to discretize and symmetrize the operator $D \tanh(h(\cdot)D)$. We assume h $2\pi-$periodic, and we apply these operators to real $2\pi-$periodic functions. Let $\mathscr{T}$ be either D or $\tanh(h(\cdot)D)$. We consider the decomposition of real $2\pi-$periodic L^2 functions f of vanishing average into even and odd components f_E, f_O, respectively. Truncations to K Fourier modes of $\mathscr{T}$ are obtained applying $\mathscr{T}$ to finite cosine and sine series

$$
f_E^K = \frac{1}{\pi} \sum_{k=1}^{K} x_k \cos kx, \quad f_O^K = \frac{1}{\pi} \sum_{k=1}^{K} y_k \sin kx, \tag{59}
$$

respectively. Since D and $\tanh(h(\cdot)D)$ map real even functions to imaginary odd functions we have

$$\mathscr{T} f_E^K = \frac{i}{\pi} \sum_{\lambda=1}^{K} x_\lambda (\mathscr{T} \cos \lambda x) = \frac{i}{\pi} \sum_{k=1}^{K} \tilde{y}_k \sin kx; \tag{60}$$

therefore,

$$\tilde{y}_k = -\frac{i}{\pi} \sum_{\lambda=1}^{K} \left(\int_0^{2\pi} \sin kx (\mathscr{T} \cos \lambda x) \mathrm{d} \right) x_\lambda. \tag{61}$$

Also, D and $\tanh(h(\cdot)D)$ map real odd functions to imaginary even functions and we similarly obtain

$$\mathscr{T} f_O^K = \frac{i}{\pi} \sum_{\lambda=1}^{K} y_\lambda (\mathscr{T} \sin \lambda x) = \frac{i}{\pi} \sum_{k=1}^{K} \tilde{x}_k \cos kx; \tag{62}$$

therefore,

$$\tilde{x}_k = -\frac{i}{\pi} \left(\sum_{\lambda=1}^{K} \int_0^{2\pi} \cos kx (\mathscr{T} \sin \lambda x) \mathrm{d} \right) y_\lambda. \tag{63}$$

We can, therefore, represent $\mathscr{T}$ on the truncated functions by the matrix

$$\begin{bmatrix} 0 & -iR \\ -iL & 0 \end{bmatrix}, \quad R_{k,\lambda} = \int_0^{2\pi} \cos kx (\mathscr{T} \sin \lambda x) \frac{\mathrm{d}}{\pi}, \quad L_{k,\lambda}$$
$$= \int_0^{2\pi} \sin kx (\mathscr{T} \cos \lambda x) \frac{\mathrm{d}}{\pi}, \tag{64}$$

$k, \lambda = 1, \ldots K$. Representing D, $\tanh(h(\cdot)D)$ by matrices M_1, M_2, respectively, obtained as above, we symmetrize numerically by considering $1/2(M_1 M_2 + M_2^T M_1^T)$, M^T the transpose of M. $M_1 M_2$ and its symmetrization are block diagonal in the odd and even subspaces. We, therefore, compute even and odd numerical eigenfunctions. By the discussion above, the discretization of the operators $\mathscr{A}_1$, $\mathscr{A}_2$, $\mathscr{A}_{1,\kappa}(\beta)$, and $\mathscr{A}_{G_{0,\kappa}}(\beta)$ follows the same scheme and leads to symmetric matrices that are block diagonal in the odd and even subspaces.

Computations of eigenvalues and eigenvectors used the Matlab implementation of the QR algorithm, see [26] also used in LAPACK. We used discretizations with $K = 2^4$ to 2^9, results in figures use $K = 2^6$. Computations by the MacBook Pro 3.1 Ghz Intel Core i5 take up to two seconds.

We now consider the operator $\mathscr{A}_{G_0}$ up to order one in β. We have

$$
\begin{aligned}
[D\tanh(h(x)D)f](x) &= -i\partial_x(2\pi)^{-1}\int_{\mathbb{R}}\tanh(h(x)k)\hat{f}(k)e^{ikx}\mathrm{d} \\
&= (2\pi)^{-1}[-i\int_{\mathbb{R}}[(\partial_x\tanh(h(x)k))\hat{f}(k)e^{ikx}\mathrm{d}k \\
&\quad + \int_{\mathbb{R}}(\tanh(h(x)k))\hat{f}(k)ke^{ikx}\mathrm{d}] \\
&= (2\pi)^{-1}[i\beta'(x)\int_{\mathbb{R}}\mathrm{sech}^2(h(x)k)k\hat{f}(k)e^{ikx}\mathrm{d} \\
&\quad + \int_{\mathbb{R}}(\tanh(h(x)k))\hat{f}(k)ke^{ikx}\mathrm{d}] \\
&= i\beta'(x)[\mathrm{sech}^2(h(x)D)Df](x) + [\tanh(h(x)D)Df](x),
\end{aligned}
\tag{65}
$$

using

$$
\partial_x(\tanh(h(x)k)) = -\mathrm{sech}^2(h(x)k)\beta'(x)k,
$$

and $\partial_x h(x) = \partial_x(h_0 - \beta(x)) = -\beta'(x)$. Furthermore,

$$
\begin{aligned}
[i\beta'(x)\mathrm{sech}^2(h(x)D)Df](x) &= i\beta'(x)(2\pi)^{-1}\int_{\mathbb{R}}[\mathrm{sech}^2(h_0k) + O(\beta^2)]k\hat{f}(k)e^{ikx}\mathrm{d} \\
&= i\beta'(x)[\mathrm{sech}^2(h_0D)D^2f](x) + O(\beta^2),
\end{aligned}
$$

and

$$
\begin{aligned}
[\tanh(h(x)D)Df](x) &= \int_{\mathbb{R}}\left(\tanh(h_0k) - \mathrm{sech}^2(h_0k)\beta(x)k + O(\beta^2)\right)\hat{f}(k)ke^{ikx}\frac{\mathrm{d}}{2\pi} \\
&= [\tanh(h_0D)Df](x) - \beta(x)[\mathrm{sech}^2(h_0D)D^2f](x) + O(\beta^2).
\end{aligned}
$$

Therefore, (65) leads to

$$
D\tanh(h(x)D) = \tanh(h_0D)D + i\beta'\mathrm{sech}^2(h_0D)D - \beta\mathrm{sech}^2(h_0D)D^2 + O(\beta^2).
$$

We also have $(\tanh(h_0D))^* = -\tanh(h_0D)$, $D^* = -D$, $(\mathrm{sech}^2(h_0D))^* = \mathrm{sech}^2(h_0D)$, $(i\beta\cdot)^* = i\beta\cdot$, $(\beta\cdot)^* = \beta\cdot$, so that

$$
\begin{aligned}
Sym(D\tanh(h(x)D)) &= D\tanh(h_0D) + \frac{1}{2}[i\beta'\mathrm{sech}^2(h_0D)D - \beta\mathrm{sech}^2(h_0D)D^2 \\
&\quad - iD\mathrm{sech}^2(h_0D)\beta' + D^2\mathrm{sech}^2(h_0D)\beta] + O(\beta^2). \quad (66)
\end{aligned}
$$

Operators $\mathrm{sech}^2(h_0D)$, $\beta\cdot$ (with β even) are real and preserve parity, while $i\beta'\cdot$, and D are imaginary and reverse parity. It follows that the operator $\mathscr{A}_2$ of (16) obtained by truncating (66) to $O(\beta^2)$ is real and preserves parity.

References

1. Aceves-Sánchez, P., Minzoni, A.A., Panayotaros, P.: Numerical study of a nonlocal model for water-waves with variable depth. Wave Motion **50**(1), 80–93 (2013)
2. Andrade, D., Nachbin, A.: A three-dimensional Dirichlet-to-Neumann operator for water waves over topography. J. Fluid Mech. **845**, 321–345 (2018)
3. Athanassoulis A. G., Papoutsellis Ch. E.: Exact semi-separation of variables in wave guides with nonplanar boundaries Proc. R. Soc. London A, 473, 20170017
4. Carter, J.D.: Bidirectional Whitham equations as models of waves in shallow water. Wave Motion **82**, 51–62 (2018)
5. Constantin, A., Escher, J.: Wave breaking for nonlinear nonlocal shallow water equations. Acta Mathematica **181**(2), 229–243 (1998)
6. Craig, W., Groves, M.D.: Hamiltonian long-wave approximations to the water-wave problem. Wave Motion **19**(4), 367–389 (1994)
7. Craig W., Guyenne P., Nicholls D.P., Sulem C.: Hamiltonian long-wave expansions for water waves over a rough bottom. In: Proc. Royal Soc. London A: Math., Phys. Eng. Sci.,46, 839-873 (2005)
8. Craig, W., Sulem, C.: Numerical simulation of gravity waves. J. Comput. Phys. **108**(1), 73–83 (1993)
9. Craig, W., Gazeau, M., Lacave, C., Sulem, C.: Bloch theory and spectral gaps for linearized water waves. SIAM J. Math. Anal. **50**(5), 5477–5501 (2018)
10. Ehrnström, M., Kalisch, H.: Traveling waves for the Whitham equation. Differ. Int. Equ. **22**(11/12), 1193–1210 (2009)
11. Ehrnström, M., Groves, M.D., Wahlénn, E.: On the existence and stability of solitary-wave solutions to a class of evolution equations of whitham type. Nonlinearity **25**(10), 2903 (2012)
12. Evans, D.V., Linton, C.M.: Sloshing frequencies. Quart. J. Mech. Appl. Math. **46**(1), 71–87 (1993)
13. Greenhill, A.G.: Wave motion in hydrodynamics (continued). Am. J. Math. **97–112**, (1887)
14. Groves, M.D.: Hamiltonian long-wave theory for water waves in a channel. Quart. J. Mech. Appl. Math. **47**, 367–404 (1994)
15. Gouin M., Ducrozet G., Ferrant P.: Development and validation of a highly nonlinear model for wave propagation over a variable bathymetry. In: ASME 2015 34th International Conference on Ocean, Offshore and Arctic Engineering, pages V007T06A077-V007T06A077. American Society of Mechanical Engineers (2015)
16. Guyenne, P., Nicholls, D.P.: Numerical simulations of solitary waves on plane slopes. Math. Comput. Simul. **69**(3), 269–281 (2005)
17. Guyenne, P., Nicholls, D.P.: A high-order spectral method for nonlinear water waves over moving bottom topography. SIAM J. Sci. Comput. **30**(1), 81–101 (2007)
18. Hur, V.M., Tao, L.: Wave breaking in shallow water model. SIAM J. Math. Anal. **50**, 354–380 (2018)
19. Hur, V.M.: Wave breaking in the Whitham equation. Adv. Math. **317**, 410–437 (2017)
20. Kuznetsov, N., Maz'ya, V., Vainberg, B.: Linear water waves: a mathematical approach. Cambridge University Press, Cambridge (2002)
21. Lamb, H.: Hydrodynamics. Cambridge University Press, Cambridge (1932)
22. Lannes D.: The water wave problem. Mathematical Surveys and Monographs, AMS, 188 (2013)
23. Macdonald, H.M.: Waves in canals. Proc. Lond. Math. Soc. **1**(1), 101–113 (1893)
24. Miles, J.W.: On Hamilton's principle for surface waves. J. Fluid Mech. **83**(01), 153–158 (1977)
25. Moldabayev, D., Kalisch, H., Dutykh, D.: The Whitham Equation as a model for surface water waves. Physica D: Nonlinear Phenomena **309**, 99–107 (2015)
26. Moler, C.B.: Numerical Computing with MATLAB: Revised Reprint. Siam (2008)
27. Naumkin P.I., Shishmarev J.A.: Nonlinear nonlocal equations in the theory of waves. A.M.S. (1994)
28. Packham, B.A.: Small-amplitude waves in a straight channel of uniform triangular cross-section. Quart. J. Mech. Appl. Math. **33**(2), 179–187 (1980)
29. Papoutsellis, C.H.E., Charalampopoulos, A.G., Athanassoulis, A.G.: Implementation of a fully non-linear Hamiltonian coupled mode theory, and application to solitary wave problem over bathymetry. Eur. J. Mech. B Fluids **72**, 199–224 (2018)
30. Porter, D., Staziker, D.J.: Extensions of the mild slope equation. J. Fluid Mech. **300**, 367–382 (1995)
31. Radder, A.C.: An explicit Hamiltonian formulation of surface waves in water of finite depth. J. Fluid Mech. **237**, 435–455 (1992)
32. Vargas-Magaña, R.M., Panayotaros, P.: A Whitham–Boussinesq long-wave model for variable topography. Wave Motion **65**, 156–174 (2016)

33. Whitham, G.B.: Linear and nonlinear waves. Wiley, Hoboken (2011)
34. Wilkening, J., Vasan, V.: Comparison of five methods to compute the Dirichlet–Neumann operator for the water wave problem. Contemp. Math. **635**, 175–210 (2015)
35. Zakharov, V.E.: Stability of periodic waves of finite amplitude on the surface of a deep fluid. J. Appl. Mech. Tech. Phys. **9**(2), 190–194 (1968)